Inorganic Chemistry

Article

pubs.acs.org/IC

Synthesis, Characterization, and Low Temperature Transport Properties of $Eu_{11-x}Yb_xCd_6Sb_{12}$ Solid-Solution Zintl Phases

Nasrin Kazem,[†] Joya Cooley,[†] Edward C. Burks,[‡] Kai Liu,[‡] and Susan M. Kauzlarich*[,†]

[†]Department of Chemistry, University of California, One Shields Ave., Davis, California 95616, United States

[‡]Department of Physics, University of California, One Shields Ave., Davis, California 95616, United States

Supporting Information

ABSTRACT: $Eu_{11-x}Yb_xCd_6Sb_{12}$ Zintl solid solutions have been prepared by tin flux reaction by employing the elements Eu/Yb/Cd/Sb/Sn in the ratio $11 - x_p:x_p:6:12:30$, where x_p is an integer less than 11 representing the preparative amount of Eu $(11 - x_p)$ and Yb (x_p). Efforts to make the Yb compositions for x exceeding ~3 resulted in structures other than the $Sr_{11}Cd_6Sb_{12}$ structure type. The crystal structures and compositions were determined by single-crystal and powder X-ray diffraction and wavelength-dispersive X-ray analysis measurements. The title solid-solution Zintl compounds crystallize in the centrosymmetric monoclinic space group $C2/m$ (no. 12, $Z = 2$) as the $Sr_{11}Cd_6Sb_{12}$ structure type (Pearson symbol mC58), and the lattice parameters decrease with increasing ytterbium content. Single crystal X-ray diffraction shows that Yb atoms are not randomly distributed in the Eu sites but have a site preference which can be attributed to size effects. The influence of the rare earth (RE) metal sites on thermal and electronic properties of $RE_{11}Cd_6Sb_{12}$ solid solutions has been studied by measuring their thermoelectric properties from 5 to 300 K after consolidation by either spark plasma sintering (SPS) or hot pressing (HP). Electron microprobe analysis reveals that some of the rare earth metal is lost during SPS; as a result pellets formed through SPS have lower electrical resistivity by an order of magnitude due to increased hole-charge carrier concentrations. While the carrier concentration increases, the mobility decreases due to deficiencies in Eu content. Refinement of powder X-ray diffraction shows that Eu loss is mainly from the Eu1 crystallographic site, which has a unique coordination suggesting that this site plays a key role in the transport properties of $RE_{11}Cd_6Sb_{12}$.

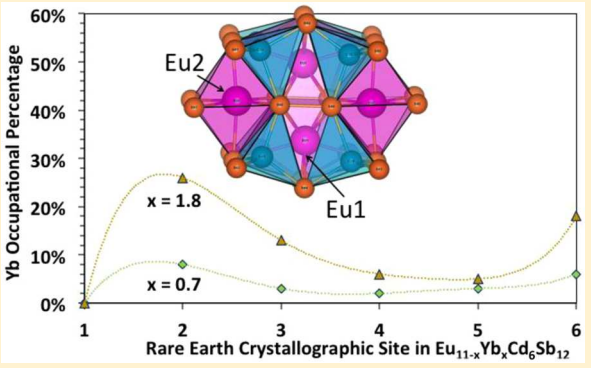

INTRODUCTION

Zintl phases are a subcategory of intermetallic compounds that are made of metals with different electronegativities.[1,2] The structures of Zintl compounds can be described as follows: the most electropositive metal donates its valence electrons to the more electronegative metal(s), which form (poly)anionic networks that satisfy the octet rule and make valence precise compounds with a small band gap. As a result of the complex structures and complicated bonding criteria (including both ionic and covalent bonding) in Zintl phases, especially in the antimonides,[3,4] very low lattice thermal conductivity is often a consequence.[2,5−10] Zintl phases have an advantage over other materials in the search for promising thermoelectrics as they already fulfill one of the required properties for high zT: low thermal conductivity.

Zintl compounds show a high flexibility in maintaining their crystal structures through compositional modifications. This provides a ready approach to optimize the electronic properties in this family of compounds by substituting either isovalent or aliovalent elements to tune the charge carrier concentration to reach high zT values.[4] Cationic sites in Zintl phases are greatly studied for alloying as they can control the charge carrier concentrations in Zintl phases through defects and subtle contributions to the electronic states; for example, in AZn_2Sb_2 (A = Sr, Ca, Eu, Yb),[11,12] charge carrier concentrations were shown to be tuned by the cation. Recently, ytterbium substitution for europium in the $Eu_{1-x}Yb_xCd_2Sb_2$ Zintl phase was shown to reduce the electrical resistivity.[13]

$Eu_{11}Cd_6Sb_{12}$ is a Zintl compound that shows exceptionally low lattice thermal conductivity of 0.78 W/mK at room temperature.[7] In addition to its glass-like lattice thermal conductivity, $Eu_{11}Cd_6Sb_{12}$ exhibits a large p-type Seebeck coefficient of ~+120 μV/K. These values are comparable to a Seebeck coefficient of ~+140 μV/K and lattice thermal conductivity of 1.7 W/mK at room temperature for state-of-the-art bulk thermoelectric material Bi_2Te_3.[14] While $Eu_{11}Cd_6Sb_{12}$ shows promising Seebeck and thermal conductivity values, the electrical resistivity is still too large to provide a promising zT. Here, we report the crystal structure and low temperature transport properties of the mixed cation phase of $Eu_{11-x}Yb_xCd_6Sb_{12}$ highlighting changes to the

Received: August 10, 2016

DOI: 10.1021/acs.inorgchem.6b01947
Inorg. Chem. XXXX, XXX, XXX−XXX

structure and the effect of consolidation on composition and properties.

EXPERIMENTAL SECTION

Synthesis. $Eu_{11-x}Yb_xCd_6Sb_{12}$ compounds were prepared by a Sn-flux synthesis technique similar to the literature procedure;[7,15] details of flux-growth synthetic procedures can be found elsewhere.[16] All manipulations were carried out in argon or nitrogen-filled glove boxes or under a vacuum to avoid oxidation. In an Ar-filled glovebox, all reagents in their elemental forms were loaded in 5 cm^3 alumina crucibles in the respective Eu/Yb/Cd/Sb/Sn molar ratios of $11 - x_p:x_p$:6:12:30 (x_p = 0, 1, and 2, which is the integer preparative amount of the Yb (and therefore $(11 - x_p)$Eu, used in the flux, and is not necessarily the same as the compositional x determined for the synthesized compound) to a total weight of ~10 g (Sources: Eu chunk, Stanford Metals, 99.99%; Yb pieces, Metall Rare Earth Limited, 99.99%; Cd pieces, Alfa, 99.98%; Sb shot, Alfa Aesar 99.9%; and Sn shot, Alfa Aesar 99.99%). The crucibles were placed into fused silica tubes with a second crucible filled with SiO_2 wool placed on top, and sealed under a pressure of less than 100 mTorr. The sealed silica tubes were heated in a box furnace at 100 °C/h to 500 °C, allowed to dwell 6 h, and then heated at 50 °C/h to 950 °C for 96 h. Subsequently, the reaction vessels were slowly cooled at 5 °C/h to 600 °C, where the molten flux was removed by inverting and spinning for 2−3 min at 6500 rpm by a centrifuge. In a N_2-filled glovebox with moisture level below 1 ppm, reaction vessels were opened and needlelike reflective crystals of $Eu_{11-x}Yb_xCd_6Sb_{12}$ compounds were observed.

Single-Crystal X-ray Diffraction. Single crystals of $Eu_{11-x}Yb_xCd_6Sb_{12}$ were selected in Paratone N oil under a microscope. The silver reflective needle-like crystal was picked by MiTeGen micro loop and then mounted on a goniometer equipped with a nitrogen stream. Single-crystal X-ray diffraction data were collected at 89 K using an APEX II X-ray diffractometer (Bruker AXS) with a CCD detector, Mo Kα radiation and a graphite monochromator. All the examined crystals from the reactions of x_p = 1 and 2 were found to have unit cell parameters similar to the $Sr_{11}Cd_6Sb_{12}$ structure type. Determinations of unit cell parameters, refinements, and raw frame data integrations were completed using the APEX II v2011.4−1 software. The centrosymmetric space group of $C2/m$ for all the samples was suggested by XPREP based on the systematic absences, and the structure was solved using direct methods from the SHELXTL version 6.14 package.[17] All six rare earth metal crystallographic sites in $Eu_{11}Cd_6Sb_{12}$ were examined for the mixed occupancies of Yb and Eu until a reasonable model with appropriate R factors, U values, and peak/hole values was achieved. Occupancies of the shared Eu/Yb sites were fixed to fully fill each crystallographic site, and they were assigned the same coordinates and atomic displacement parameters.

Powder X-ray Diffraction (PXRD). PXRD patterns were collected on a BRUKER model D8 diffractometer in Bragg−Brentano reflection geometry with Cu Kα radiation (λ = 1.5418 Å) for 2θ = 20−80° at room temperature in the air. The program JANA 2006 was used to perform profile matching by employing pseudo-Voigt axial divergence asymmetry peak shape for the calculated patterns.[18] The structures from the single crystal X-ray diffraction experiments were used as the starting structural model that matched very well with the intensities and the positions of the experimentally observed peaks.

Electron Microprobe Analysis (EMPA). Single crystals and pellet samples of $Eu_{11-x}Yb_xCd_6Sb_{12}$ were enclosed in epoxy and polished to provide flat surfaces for analysis. The polished samples were mounted on 25 mm metal rounds using adhesive carbon tape and were carbon coated to make them conducting. Microprobe analysis was performed using a Cameca SX-100 Electron Probe Microanalyzer with wavelength-dispersive spectrometers. Back scattered electrons were used for imaging the surfaces of the samples. Characteristic X-rays generated by samples were analyzed by wavelength-dispersive spectroscopy to determine the compositions, and element mapping was accomplished to assess the spatial distribution of elements in the samples. X-ray intensities of Eu, Yb, Cd, Sb, and Sn were compared with the calibrated standards $EuPO_3$, Yb_2O_3, Cd (metal), Sb (metal), and Sn (metal) for quantitative analysis. At least 15 different points with a spot size of 1 μm were analyzed for each sample. Electron maps for both single crystals and two of the pressed pellets are provided in the Supporting Information.

Sample Preparation for Transport Properties. The pristine sample was a diamond cut plate (2 × 3 mm^2 and 1 mm thickness) of the pellet created by hot pressing (HP) and was previously reported.[7] Polycrystalline samples of $Eu_{11-x}Yb_xCd_6Sb_{12}$ (mass: ~1.5 g) were ground in the glovebox and transferred into a 12.7 mm high-density graphite die (POCO). The sample was first cold pressed at 2 kN at room temperature under a partial pressure of Ar inside the Dr. Sinter Lab Jr. SPS-211Lx spark plasma sintering (SPS) system (Sumitomo, Tokyo, Japan). Temperature was increased from room temperature to 490 °C in 9 min, then to 500 °C in 1 min, where it dwelled for 10 min. Beginning at ~420 °C, the loading force was increased from 2 kN to 11 kN. The sample was cooled to room temperature followed by the release of the uniaxial force to ~0.3 kN. The geometrical sample density of the pellet was >85% of the crystallographic value. The purity of the samples after SPS was verified by powder X-ray diffraction, and the patterns were in good agreement with the positions of the calculated Bragg reflections for the crystallographic structure.

Physical Properties Measurements System (PPMS). Transport properties of diamond cut $Eu_{11-x}Yb_xCd_6Sb_{12}$ pellets were studied by using a commercial multipurpose measurement device (Quantum Design PPMS) over the temperature range of 2−300 K. The Seebeck coefficient and thermal conductivity were measured using the thermal transport option (TTO). For TTO measurement, pellets were cut to volumes of 25.76, 28.92, and 23.56 mm^3 for samples x_p = 0, 1 and 2, respectively. AC transport/electrical resistivity was measured using a standard four-point alternating-current technique to exclude resistance of the leads. For AC transport, pellets had heights of 1.20, 1.74, and 1.52 mm for samples x_p = 0, 1, and 2, respectively.

Hall Measurements. Hall measurements were performed at room temperature using the Van der Pauw method. Electrical contact was made to the four corners of each sample using silver paint and platinum wire. Magnetic fields up to 1.5T were applied using the electromagnet from a PMC 3900 Vibrating Sample Magnetometer. DC current of 100 mA was applied using a Keithley 6221 current source and Hall Voltage measured with a Keithley 2182A nanovoltmeter. Hall coefficients, R_H, were calculated using the sample thickness and the slope of a linear fit to R vs H data where H is the applied field. Carrier concentrations were calculated as $n_H = 1/eR_H$ where e is the fundamental charge.

RESULTS AND DISCUSSION

Structure Description. Single crystals of $Eu_{11-x}Yb_xCd_6Sb_{12}$ ($x \sim 0.4$ and 1) were synthesized by tin flux reaction and crystallized in the monoclinic space group $C2/m$ with the $Sr_{11}Cd_6Sb_{12}$ structure type, containing 15 crystallographically unique sites in the asymmetric unit (6 RE = rare earth (Eu, Yb); 6 Sb and 3 Cd sites).[19] These are special positions of the 4i Wyckoff position, except for RE6, located in the 2a Wyckoff site. Single-crystal and powder X-ray diffraction studies revealed that the $Sr_{11}Cd_6Sb_{12}$ structure type is not maintained for $Eu_{11-x}Yb_xCd_6Sb_{12}$ ($x \geq 3$), and the simpler $Eu_{2-x}Yb_xCdSb_2$ structure published by Saparov et al. is obtained.[20] Only $Eu_{11-x}Yb_xCd_6Sb_{12}$ ($x \leq 2$) compounds that crystallize in the $Sr_{11}Cd_6Sb_{12}$ structure type are considered in this paper. All the structure refinements resulted in satisfactory R_1 and wR_2 values (R_1 < 2.5% and wR_2 < 5.0%); CIFs (Crystallographic Information Files) can be found in the Supporting Information (SI). Refinement of occupancies provides $x_{Cryst} \sim 0.4$ and 1.0 where x_{Cryst} indicates the amount of Yb/formula determined through the refinement of the single crystal X-ray diffraction data. The average compositions from EMPA on single crystals, shown in Table 1, also are indicative of the formation of Zintl phase $Eu_{11-x}Yb_xCd_6Sb_{12}$ with $x \sim 0.3$ and 0.9 for x_p = 1 and 2,

DOI: 10.1021/acs.inorgchem.6b01947
Inorg. Chem. XXXX, XXX, XXX−XXX

Table 1. Compositions with Standard Deviations in Parentheses Obtained from Elemental Analysis by EMPA on Single Crystals and HP/SPS Pressed Pellets of $Eu_{11-x}Yb_xCd_6Sb_{12}$

	single crystal		pellet	
	composition	Yb+Eu	composition	Yb+Eu
$x_p = 0$	$Eu_{10.95(7)}Cd_{6.03(5)}Sb_{12.01(2)}$ [7]	10.95(7)	(HP) $Eu_{10.95(6)}Cd_{6.01(5)}Sb_{12.04(2)}$ [7]	10.95(6)
			(SPS) $Eu_{10.78(1)}Cd_{5.99(7)}Sb_{12.0(1)}$	10.78(1)
$x_p = 1$	$Eu_{10.71(8)}Yb_{0.26(2)}Cd_{6.02(3)}Sb_{12.01(6)}$	10.97(6)	(SPS) $Eu_{10.0(1)}Yb_{0.73(8)}Cd_{6.10(6)}Sb_{11.91(3)}$	10.72(4)
$x_p = 2$	$Eu_{10.00(9)}Yb_{0.93(5)}Cd_{6.03(6)}Sb_{12.02(7)}$	10.94(8)	(SPS) $Eu_{8.43(1)}Yb_{1.8(3)}Cd_{6.06(7)}Sb_{11.97(1)}$	10.3(2)

respectively, in agreement with the composition from single crystal refinement. There is no evidence of Sn substitution in the structure either by the crystal structure refinements or by the EMPA elemental analysis.

As a Zintl crystal structure comprised of metals with different electronegativities, $Eu_{11-x}Yb_xCd_6Sb_{12}$ can be described as $[Cd_6Sb_{12}]^{-22}$ double pentagons connected to each other in the *b* direction and forming 1-D extended anionic tunnels as shown in Figure 1. Rare earth atoms can be considered as filling the space inside the double pentagons and between them, providing the electrons needed for the covalent bonds in the polyanionic network to satisfy the octet rule. On the basis of the Zintl formalism, the structure can be considered a valence precise compound: $(RE^{2+})_{11}[(4b\text{-}Cd^{2-})_6(1b\text{-}Sb^{2-})_2(2b\text{-}Sb^{1-})_6(3b\text{-}Sb^0)_4]$ by assigning three-bonded Sb atoms (3*b*-Sb), two-bonded Sb atoms (2*b*-Sb), and one-bonded Sb atoms (1*b*-Sb) as Sb^0, Sb^{1-}, and Sb^{2-}, respectively. The lattice parameters decrease with increasing Yb content (determined from single-crystal X-ray diffraction), consistent with the smaller metallic radii of Yb (1.78 Å) as compared to Eu (1.83 Å).[20] The site occupancy factors for each rare earth metal site are freely refined in order to determine the presence of vacancies. All the unrestricted refinements for the rare earth sites lead to an unstable refinement except for Eu1 that is only occupied by Eu and shows no evidence of the vacancy (discussed later). The EMPA results on the solid solution single crystals show that less rare earth sites are nearly fully occupied. This is consistent with the composition from EMPA data on the single crystal samples, $Eu_{10.95(7)}Cd_{6.03(5)}Sb_{12.01(2)}$, reported in our previous study showing no crystallographic evidence for vacancies.[7] As a result, it can be concluded that Eu and Yb almost fully occupy the rare earth crystallographic sites in the solid solution single crystals.

Site occupancy refinements of single-crystal X-ray diffraction data show that Yb substitution on the RE sites is not random. Figure 1 shows qualitatively the Yb fractional site of occupancy by the ratio of the sky blue (Yb) wedge to the pink color (Eu) wedge in each RE site numerically listed in Figure 2. As a result

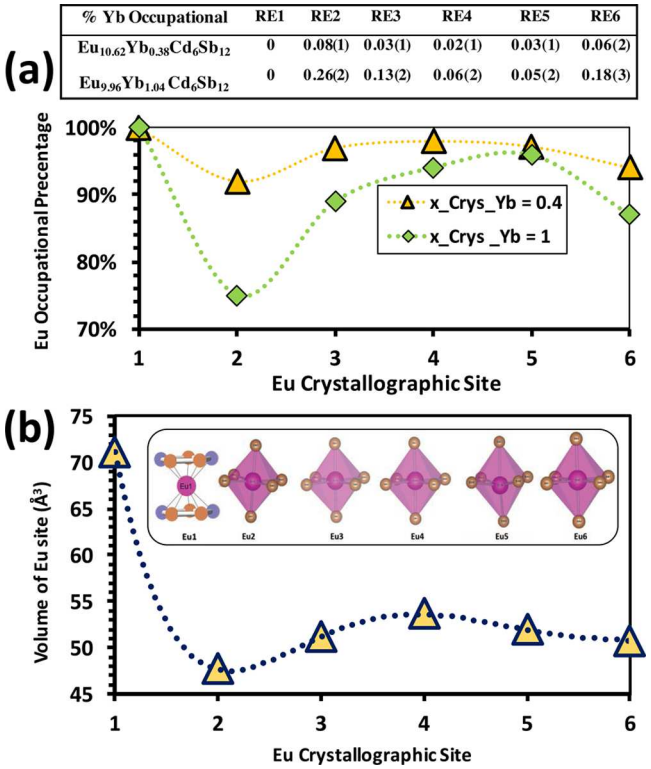

Figure 2. (a) Eu occupancy at the rare earth crystallography sites show the same trend for $Eu_{11-x}Yb_xCd_6Sb_{12}$, $x_{Cryst} \sim 0.4$ and $x_{Cryst} \sim 1$. Site occupancy percentage factors for Yb (and standard deviations) in the six crystallographic positions of rare earth atoms in $Eu_{11-x}Yb_xCd_6Sb_{12}$ listed at the top of the plot. (b) The calculated volume of each of the six crystallographic Eu sites in $Eu_{11}Cd_6Sb_{12}$ shows that the Eu2 polyhedron is the smallest and Eu1 is the largest. Coordination spheres of all six crystallographically independent Eu sites in $Eu_{11}Cd_6Sb_{12}$ are shown on top. The coordination sphere cutoff has been set at 4 Å.

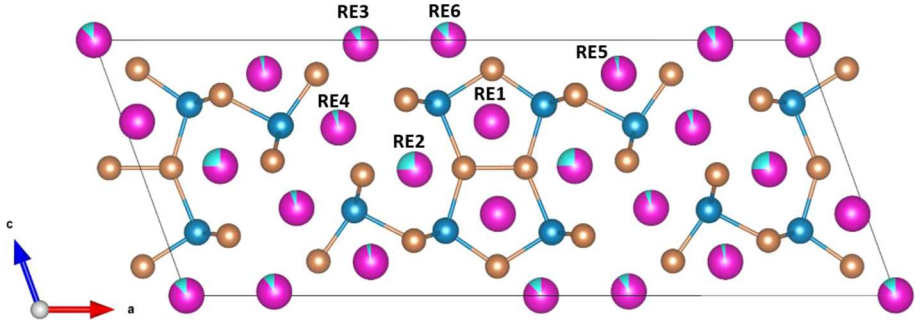

Figure 1. A view of the crystal structure of $Eu_{11-x}Yb_xCd_6Sb_{12}$ ($x_{Cryst} \sim 1$) down the *b* axis. The anionic network is made of the $[Cd_6Sb_{12}]^{-22}$ double pentagons extended in the *b* direction forming isolated tunnels filled by Eu1 atoms (blue spheres = Cd; orange spheres = Sb; pink spheres = Eu; sky blue wedge = the fraction of Yb occupation at Eu sites). There is a nonrandom distribution of Yb at Eu sites with the highest Yb substitution at Eu2 and no substitution at Eu1 sites.

DOI: 10.1021/acs.inorgchem.6b01947
Inorg. Chem. XXXX, XXX, XXX−XXX

of "coloring" of the cation sites,[7,21] some Eu positions are more favored for substitution than others. There are six different crystallographic sites for Eu (shown in Figure 2) that can be substituted by Yb atoms. Figure 2a shows that refined Yb occupancy factors for both $Eu_{11-x}Yb_xCd_6Sb_{12}$ (x_{Cryst} = 0.4 and 1) compounds follow the same preferential Yb substitution trend in rare earth sites RE2 > RE6, RE3 > RE4, and RE5 > RE6. This preferential substitution can be explained by simple geometrical reasoning. A close look at each Eu site reveals that only the Eu1 site has a distinct coordination environment of eclipsed ferrocene-like geometry compared to the other Eu sites; Eu1 is sandwiched between two pentagonal rings made of Cd and Sb atoms (see Figure 2b). The other five Eu sites show the pseudo-octahedral geometry: six Sb atoms surrounding each of the Eu sites. All six Eu coordination spheres are shown in Figure 2b. The results from the refined single-crystal X-ray diffraction structures show that only the sites with octahedral coordination of Sb are inhabited by the smaller cation, Yb^{2+}, while the eclipsed ferrocene arrangement of Cd−Sb pentagons remains intact with only Eu^{2+}. The calculated volumes (calculated in *VESTA*[22]) of each Eu site in $Eu_{11}Cd_6Sb_{12}$ follow the trend Eu2 < Eu3 < Eu4 < ... < Eu1, suggesting that the smaller polyhedra are favored by smaller Yb (Figure 2b). This result is consistent with the unsuccessful attempts to make a Ca analogue of $Eu_{11}Cd_6Sb_{12}$ while the Sr analogue exists, suggesting that the size effects are the dominant stability factor for this structure.[19] Careful examination shows that not all the bond distances are reduced by the Yb substitutions. Through the main substitution of Yb at Eu2 crystallographic sites (see Table 2 and Figure 3), all six RE2−Sb bonds at this pseudo-octahedral RE site become smaller. However, the other bond distances such as Sb5−Sb5 and Eu1−Sb bond lengths remain fairly intact all over the substitutional alloyed structure.

Table 2. Selected Bond Distances in $Eu_{11-x}Yb_xCd_6Sb_{12}$ Solid Solutions

$Eu_{11-x}Yb_xCd_6Sb_{12}$	x = 0	$x \approx 0.4$	$x \approx 1$
2 × (Eu2−Sb5)	3.276(1) Å	3.272(4) Å	3.262(4) Å
2 × (Eu2−Sb1)	3.216(1) Å	3.210(5) Å	3.199(6) Å
Eu2−Sb3	3.382(1) Å	3.378(4) Å	3.367(4) Å
Eu2−Sb2	3.250(1) Å	3.245(5) Å	3.238(6) Å
Sb5−Sb5	2.812(1)Å	2.815(8) Å	2.818(9) Å
Cd3−Sb5	3.186(9)Å	3.182(6) Å	3.177(8) Å
2 × (Eu1−Sb5#1)	3.417(1) Å	3.415(4) Å	3.412(4) Å
2 × (Eu1−Sb5#2)	3.517(1) Å	3.516(4) Å	3.515(4) Å
2 × (Eu1−Sb4)	3.358(5)Å	3.358(4) Å	3.360(4) Å

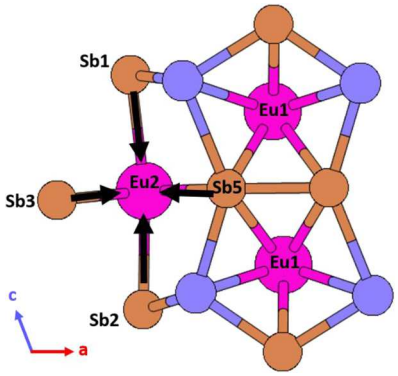

Figure 3. Schematic illustrating how certain chemical bonds are affected by Yb substitution. One-sided black arrows show the bond length is decreasing.

Sample Consolidation and Characterization. The polycrystalline pellets of solid solutions of $Eu_{11-x}Yb_xCd_6Sb_{12}$ ($x \sim 0$, 1, and 2) were formed by the spark plasma sintering (SPS) of pulverized solid solution crystal samples. The consolidated samples show geometrical densities higher than 85%. The average compositions from EMPA on pellets, shown in Table 1, indicate that the major phase belongs to the $Eu_{11-x}Yb_xCd_6Sb_{12}$ Zintl phase composition with x = 0, 0.7, and 1.8, and these compositions will be used for the rest of the discussion in this paper. The EMPA shows a considerable loss of rare earth metal atoms after consolidation of the samples by SPS as the summation of Eu and Yb does not maintain 11 atoms per formula (see the last column in Table 1). The comparison between the total rare earth metals/formula unit in each SPS pellet and its corresponding composition from the single crystals shows that the loss of the rare earth metals becomes more significant at higher Yb concentration, ~2% for $x \sim 0.7$ and more than 6% for $x \sim 1.8$. The rare earth metal loss is not observed by hot pressing (HP) of the undoped $Eu_{11}Cd_6Sb_{12}$. The rate and method of sample heating in SPS contributes to vaporization of the sample. The vaporization only affects the cation content of the samples, based on the elemental composition determined from EMPA.

The EMPA studies show the presence of the minor phase $Eu_{2-x}Yb_xCdSb_2$ (2−1−2) in the pressed pellets. The pulverized pressed pellets have been studied by PXRD for structural studies of the samples after consolidation. Representative patterns of the x = 0, 0.7, and 1.8 samples of $Eu_{11-x}Yb_xCd_6Sb_{12}$ are shown in Figure 4. The best profile matching was achieved by using the $Sr_{11}Cd_6Sb_{12}$ (11−6−12) structure type solved for single crystals of each reaction and the Yb_2CdSb_2 structure type (2−1−2) impurity phase.[23] The corresponding calculated patterns are shown as orange lines overlaid on each observed pattern, shown in black, with the Bragg positions for each phase. The complete match of the calculated and experimental patterns indicates that the peaks are fully matched with the patterns of 11−6−12 and 2−1−2 structures. Note that the x = 0 pattern is fit with only the 11−6−12 structure type, and there is no evidence for the presence of the 2−1−2 phase. LeBail Profile fitting suggests the presence of less than 5 and 25 vol % of the 2−1−2 impurity phase in x = 0.7 and x = 1.8 pressed pellet samples, respectively. PXRD results show that despite the loss of rare earth atoms during sample pressing, the $Sr_{11}Cd_6Sb_{12}$ crystal structure is favorably preserved. As previously mentioned, the extent of the rare earth metal loss becomes greater by increasing the Yb content of the structure when the samples have been pressed under the same conditions. It suggests the dependency of the rare earth metal loss on both the sintering technique and the composition (Yb concentration).

Rietveld refinement of the powder X-ray diffraction data was attempted through atomic coordination and displacement parameter (ADP) refinements for all the elements in the main phase with the $Sr_{11}Cd_6Sb_{12}$ structure for x = 0 and 0.7. The x = 1.8 sample was not further analyzed by Rietveld refinement because of the presence of a significant amount of the secondary phase, $Eu_{2-x}Yb_xCdSb_2$. During the ADP refinement, a few atoms with negative ADP were replaced with positive ADP values of similar atoms since a negative temperature factor has no physical meaning. Although, it shows

DOI: 10.1021/acs.inorgchem.6b01947
Inorg. Chem. XXXX, XXX, XXX−XXX

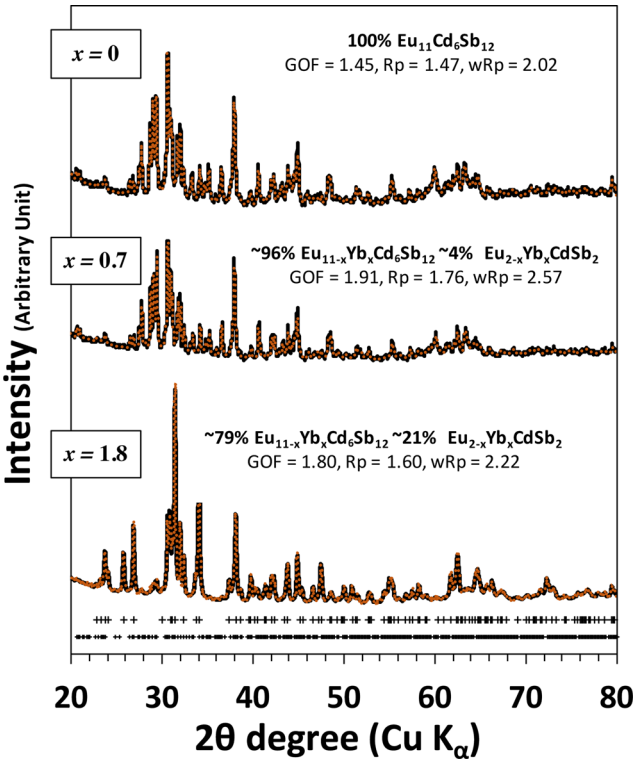

Figure 4. Le Bail profile refinements of powder X-ray diffraction patterns for $Eu_{11-x}Yb_xCd_6Sb_{12}$ (x = 0, top pattern; x = 0.7, middle pattern; and x = 1.8, lower pattern) with the location of individual Bragg reflections for both major and minor phases below and their corresponding statistical values of refinements.

the necessity of higher quality powder data with more reliable intensities to analyze further, the refinements resulted in the highest ADP for the crystallographic Eu1 site, which is more than 1 order of magnitude larger than those from the other Eu sites, can be indicative of the vacancy at this position. To ensure any certain conclusions about occupancies, more detailed studies are required.

Transport Properties of $Eu_{11-x}Yb_xCd_6Sb_{12}$. $Eu_{11}Cd_6Sb_{12}$ behaves as an extrinsic p-type degenerate semiconducting material with a relatively high Seebeck coefficient of ~+120 μV/K at room temperature which coincides with a relatively high electrical resistivity of ~6 mΩ·cm leading to low thermoelectric efficiencies.[7,15] Charge carrier concentration has been selected as a variable to be modified to decrease the resistivity of $Eu_{11}Cd_6Sb_{12}$. Here, we substitute Yb in Eu crystallographic sites to reduce the electrical resistivity as slightly higher electronegativity of Yb can induce more positive charges (holes) in the structure as supported by the other studies on $Yb_xEu_{1-x}Cd_2Sb_2$ Zintl compound. In the case of $Yb_xEu_{1-x}Cd_2Sb_2$,[13] lower resistivity is achieved through increasing both mobility and positive charge carrier concentration by Yb substitution in Eu sites, suggesting that the smaller Yb can both provide more positive charges and a better orbital overlap.

Temperature-dependent electrical resistivity (ρ) of $Eu_{11-x}Yb_xCd_6Sb_{12}$ (x = 0, 0.7 and 1.8) and $Eu_{11}Cd_6Sb_{12}$ are shown in Figure 5; for the sample, $Eu_{11}Cd_6Sb_{12}$, the measurements are performed to 2 K. Resistivity of all samples increases approximately linearly with increasing temperature showing that all samples are metallic. For the pristine sample, there is an increase in electrical resistivity at T ~ 7.5 K where

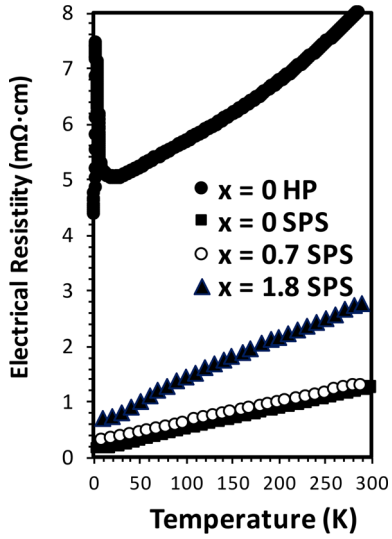

Figure 5. Temperature dependence of electrical resistivity for $Eu_{11}Cd_6Sb_{12}$ and $Eu_{11-x}Yb_xCd_6Sb_{12}$ (x = 0, 0.7, and 1.8).

the material experiences an antiferromagnetic ordering (T_N = 7.5 K). By isovalent substitution of Yb^{2+} for Eu^{2+}, only a subtle manipulation of charge carrier concentration due to the slightly different electronegativity of Yb and Eu atoms is expected. This simple approach has been employed in many Zintl compounds for finely tuning the charge carrier concentration.[7,13,15,20,24,25] As Figure 6 shows, the electrical resistivity values of the SPS

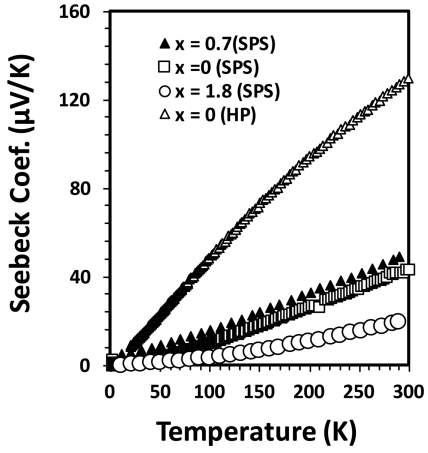

Figure 6. Temperature dependence of Seebeck coefficient for $Eu_{11-x}Yb_xCd_6Sb_{12}$ compounds.

samples are significantly lower than the HP sample; the undoped SPS sample is 6 times more conductive than the HP analogue at room temperature. The dependence of the electronic properties on the sample preparation is expected as a result of the different compositions formed during HP and SPS, discussed earlier. Within the SPS prepared solid solution samples, resistivity is correlated with both x and the nonstoichiometry of the composition as the resistivity first increases by substituting Yb for Eu in x = 0.7 (low defects) and then decreases by substituting more Yb in x = 1.8 (high defects).

To better understand the trend in these solid solutions, Hall coefficient measurements at room temperature were carried out with the Van der Pauw (VDP) technique, as summarized in

DOI: 10.1021/acs.inorgchem.6b01947
Inorg. Chem. XXXX, XXX, XXX−XXX

Table 3. The positive Hall coefficients of samples reveal that holes are the dominant carriers at room temperature which is in agreement with the positive Seebeck coefficients (vide infra). Hall measurements indicate that the carrier concentration increased for the SPS samples as expected from the off-stoichiometric compositions, confirmed by EMPA data shown in Table 1. The solid solution $Eu_{11-x}Yb_xCd_6Sb_{12}$ with x = 0, 0.7, and 1.8 shows 1 to 2 orders of magnitude higher hole concentrations, compared to the more electron precise, x = 0, HP sample. These higher charge carrier concentrations are consistent with the loss of ~2.5% and 6% Eu in the x = 0.7 and 1.8 samples, respectively (Table 1), that introduces ~0.5 and 1.4 h^+ charge carriers per formula, corresponding to ~6.2×10^{20} and 1.6×10^{21} carriers/cm^3. Greater rare earth metal loss in x = 1.8 can be due to the size mismatch of Eu^{2+}(1.83 Å) and Yb^{2+} (1.78 Å)[26] that may make solid solutions with higher Yb contents less stable and more prone to losing Eu from the larger Eu crystallographic site, Eu1. Furthermore, as Table 3 shows, Hall mobility decreases drastically as the composition changes for the SPS samples, up to an order of magnitude for $Eu_{11-x}Yb_xCd_6Sb_{12}$ (x = 1.8) compared to the compositionally exact HP sample.

Table 3. Resistivity, ρ, Carrier Concentration n_H, and Hall Mobility μ_H of $Eu_{11-x}Yb_xCd_6Sb_{12}$ Solid Solutions at Room Temperature (*n_H and μ_H for HP x = 0 Sample Are from ref 12)

	x = 0			
$Eu_{11-x}Yb_xCd_6Sb_{12}$	HP	SPS	x = 0.7 SPS	x = 1.8 SPS
ρ(300 K), mΩ·cm	8.2	1.6	2.8	1.2
n_H (300 K, cm^{-3})	2×10^{19}*	3×10^{20}	2×10^{20}	2×10^{21}
μ_H [300 K, $cm^2/(V{\cdot}s)$]	30*	13	10	3

Rietveld refinement of the powder X-ray diffraction data indicated that the Eu1 site has considerable vacancy. Previously, DOS of the pristine structure of $Eu_{11}Cd_6Sb_{12}$ showed that as long as the Eu1−Sb4 orbital overlap is maintained, high mobility for charge carriers can be guaranteed. For example, substitution of the smaller As at Sb sites resulted in very poor orbital overlap of Eu1−As4 and as a result low charge carrier mobility.[7] However, the substitution of Zn at Cd sites makes the unit cell smaller in the b direction, where Eu1 and Sb4 interaction occurs, increasing Eu1−Sb4 overlap and causing higher charge carrier mobility.[15] Here, based on the single crystal and powder refinement, the "coloring problem"[21] resulted in no substitution of smaller Yb in the Eu1 site. This site specific substitution is also reflected in the slight decrease of the b crystallographic parameters of 4.7294(2), 4.7269(3), and 4.7242(3) Å in $Eu_{11-x}Yb_xCd_6Sb_{12}$ (x_{Cryst} = 0, 0.4, and 1) compounds, respectively.

The applied sintering technique is therefore the main parameter influencing the transport properties in this series of compounds, causing a loss of Eu and consequently a higher concentration of holes in this solid solution. As the Eu is mostly lost from the Eu1 crystallographic site and because the mobility of holes is drastically reduced, it is likely that the orbital interaction of Eu1−Sb4 has an important role in the transport properties of the 11−6−12 structure type. The resistivity results of solid solution samples were reproduced with two different samples, showing consistency in the resistivity data.

Temperature dependent Seebeck coefficients of $Eu_{11-x}Yb_xCd_6Sb_{12}$ (x = 0, 0.7, and 1.8) compounds are shown in Figure 6. The positive Seebeck coefficients of all samples in the measured temperature range suggest that holes are the dominant carrier type, in agreement with Hall measurements. For the SPS solid solution samples, the Seebeck coefficient increases approximately linearly with increasing temperature from 10 K to room temperature, consistent with the metallic behavior observed by electrical resistivity. As expected, the Seebeck coefficients decrease with increasing charge carrier concentration in SPS samples. As a result, the undoped sample and $Eu_{11-x}Yb_xCd_6Sb_{12}$ (x = 1.8) exhibit the highest and the lowest Seebeck coefficients, respectively.

The total thermal conductivities (κ_{total}) of $Eu_{11-x}Yb_xCd_6Sb_{12}$ (x = 0, 0.7 and 1.8) compounds are shown in Figure 7a.

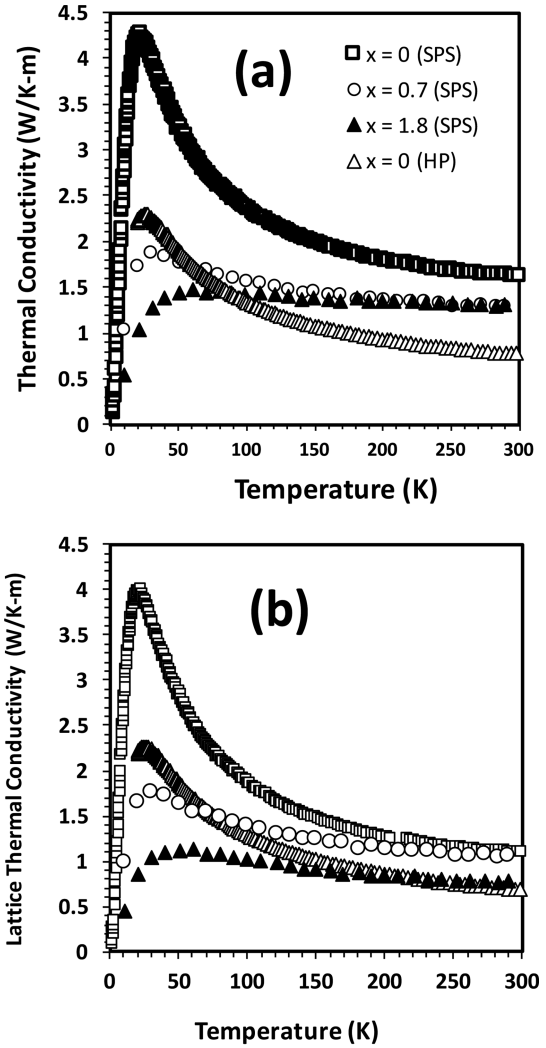

Figure 7. (a) The total thermal conductivity, κ_{total}, and (b) lattice thermal conductivity, $\kappa_{lattice} = \kappa_{total} - \kappa_e$(same legend for both), in samples of $Eu_{11-x}Yb_xCd_6Sb_{12}$ are shown. L values were estimated from the $L = 1.5 + \exp[-|\alpha|/116]$ equation.

Thermal conductivity in all samples rapidly increases from 10 to ~30 K and then decreases slowly with increasing temperature, creating a peak at around 40 K, which is typical for crystalline materials.[27] All samples show low thermal conductivities ranging from ~0.77 to 1.6 Wm^{-1} K^{-1} at room temperature. The total thermal conductivities for the SPS samples between room temperature and ~100 K are higher than the HP sample due to the larger electronic contribution in

DOI: 10.1021/acs.inorgchem.6b01947
Inorg. Chem. XXXX, XXX, XXX−XXX

thermal conductivity as a result of their low electrical resistivity. The $Eu_{11}Cd_6Sb_{12}$ sample (HP) has the lowest thermal conductivity up to 100 K where the sharp rise in thermal conductivity happens for all the samples. At temperatures lower than 100 K, the solid solution of $x = 1.8$ (SPS) shows the lowest thermal conductivity. Two primary mechanisms contribute to the total thermal conductivity: lattice (phonon) and electronic, $\kappa_{total} = \kappa_e + \kappa_{lattice}$. The electronic contribution can be estimated from $\kappa_e = LT/\rho$, where T is temperature, ρ is electrical resistivity, and L is the Lorenz number. Lorenz numbers are estimated as $L = 1.5 + \exp[-|\alpha|/116]$ rather than as a classic constant value to consider the temperature dependence, improving the estimate of lattice thermal conductivity.[28] These calculated L values at room temperature for the SPS samples are close to the result given by the free electron model, 2.45×10^{-8} $W\Omega K^{-2}$. This is a good estimate as their electrical resistivities are relatively low and the L value (at room temperature) for the pristine HP compound is smaller (around 1.75×10^{8} $W\Omega K^{-2}$) as it is less conductive than the solid solutions. Subtraction of the electronic contribution from the total thermal conductivity, $\kappa_{total} - \kappa_e$, gives the lattice contribution ($\kappa_{lattice}$). The electronic contribution in total thermal conductivities becomes less prominent when temperature decreases, so at low temperature, $\kappa_{total} \rightarrow \kappa_{lattice}$. Within the SPS samples, the lattice thermal conductivity decreases by substituting the Yb into the structure as expected through alloying techniques.

The values of the thermoelectric figure of merit $zT = \alpha^2 T/\kappa\rho$ for the $Eu_{11-x}Yb_xCd_6Sb_{12}$ samples were calculated from the polynomial fits for ρ, κ, and α curves. These figures of merit are shown as a function of temperature in Figure 8. SPS

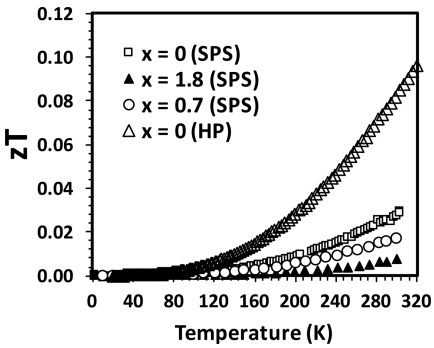

Figure 8. Curves of figure of merit for $Eu_{11-x}Yb_xCd_6Sb_{12}$ solid solutions.

$Eu_{11-x}Yb_xCd_6Sb_{12}$ samples do not provide highly efficient thermoelectrics because of the deterioration of the Seebeck coefficient as a result of the significant loss of Eu atoms during SPS sintering. This declining Seebeck coefficient is not compensated by the decreased electrical resistivity as the mobility is also significantly suppressed. The transport property measurements results in $zT \sim 0.1$ for undoped $Eu_{11}Cd_6Sb_{12}$ at room temperature. This is slightly larger than, but within standard deviation of, our previously reported zT of 0.07 at room temperature.[7]

CONCLUSIONS

Yb atoms are substituted into Eu sites of $Eu_{11}Cd_6Sb_{12}$ Zintl compound, and the thermal and electronic properties are studied by investigating the trends of the low temperature thermoelectric properties of the $Eu_{11-x}Yb_xCd_6Sb_{12}$ ($x = 0$, 0.7 and 1.8) system. Attempts to increase the amount of Yb ($x \geq 3$) were unsuccessful and led to phase separation, suggestive of a small phase width. Single crystal X-ray diffraction refinements show that Yb atoms are not randomly distributed in six unique crystallographic Eu sites, showing that $Eu_{11-x}Yb_xCd_6Sb_{12}$ is an example of "coloring" chemical substitution. Some of the site preference can be attributed to size differences between Eu and Yb. Transport properties of the $Eu_{11-x}Yb_xCd_6Sb_{12}$ samples at low temperatures up to 300 K are measured on consolidated bulk samples formed by either SPS or HP. The SPS process leads to loss of cation (Eu) and defects in the sample. High positive charge carrier concentration is introduced by the Eu loss in SPS samples. Regardless of the significant Eu loss, PXRD is consistent with the 11−6−12 structure type, and the crystallographic Eu1 site is primarily affected. The Eu loss at the Eu1 site along with lower mobility for the SPS samples is consistent with the interpretation of disruption of Eu1−Sb4 interactions, which is proposed as key for transport of charge carriers in 11−6−12 family. Higher Yb contribution in the composition causes higher Eu loss and subsequently a higher charge carrier concentration and lower mobility. Although the electrical resistivity decreases by substituting Yb in Eu sites, the Seebeck depreciation is not compensated, resulting in low zT values for $Eu_{11-x}Yb_xCd_6Sb_{12}$ solid solutions.

ASSOCIATED CONTENT

Supporting Information

CIF of $Eu_{11-x}Yb_xCd_6Sb_{12}$ ($x = 0.4$ and 1) solid solutions. (pdf). The Supporting Information is available free of charge on the ACS Publications website at DOI: 10.1021/acs.inorgchem.6b01947.

Elemental maps for single crystals and pressed pellets (PDF)

CIF of $Eu_{11-x}Yb_xCd_6Sb_{12}$ ($x = 0.4$ and 1) solid solutions (CIF)

CIF of $Eu_{11-x}Yb_xCd_6Sb_{12}$ ($x = 0.4$ and 1) solid solutions (CIF)

AUTHOR INFORMATION

Corresponding Author

*E-mail: smkauzlarich@ucdavis.edu.

Notes

The authors declare no competing financial interest.

ACKNOWLEDGMENTS

We thank Dr. Sarah Roeske and Nick Botto for assistance with microprobe analysis. This research was funded by GAANN fellowships (N.K. and J.C.), NSF DMR-1405973 and DMR-1543582.

REFERENCES

(1) Janka, O.; Kauzlarich, S. M. Zintl Compounds. In *Encyclopedia of Inorganic and Bioinorganic Chemistry*; John Wiley & Sons, Ltd: New York, 2011.

(2) Kazem, N.; Hurtado, A.; Klobes, B.; Hermann, R. P.; Kauzlarich, S. M. $Eu_9Cd_{4-x}CM_{2+x-y}\square_ySb_9$: $Ca_9Mn_4Bi_9$-Type Structure Stuffed with Coinage Metals (Cu, Ag, and Au) and the Challenges with Classical Valence Theory in Describing These Possible Zintl Phases. *Inorg. Chem.* **2014**, *54*, 850−859.

(3) Cooley, J.; Kazem, N.; Zaikina, J. V.; Fettinger, J. C.; Kauzlarich, S. M. Effect of Isovalent Substitution on the Structure and Properties

DOI: 10.1021/acs.inorgchem.6b01947
Inorg. Chem. XXXX, XXX, XXX−XXX

of the Zintl Phase Solid Solution $Eu_7Cd_4Sb_{8-x}As_x$ ($2 \le x \le 5$). *Inorg. Chem.* **2015**, *54*, 11767−11775.
(4) Kazem, N.; Kauzlarich, S. Thermoelectric Properties of Zintl Antimonides. *Handbook on the Physics and Chemistry of Rare Earths* **2016**, *50*, 177.
(5) Brown, S. R.; Kauzlarich, S. M.; Gascoin, F.; Snyder, G. J. $Yb_{14}MnSb_{11}$: New High Efficiency Thermoelectric Material for Power Generation. *Chem. Mater.* **2006**, *18*, 1873−1877.
(6) Bux, S. K.; Zevalkink, A.; Janka, O.; Uhl, D.; Kauzlarich, S.; Snyder, J. G.; Fleurial, J.-P. Glass-like lattice thermal conductivity and high thermoelectric efficiency in $Yb_9Mn_{4.2}Sb_9$. *J. Mater. Chem. A* **2014**, *2*, 215−220.
(7) Kazem, N.; Xie, W.; Ohno, S.; Zevalkink, A.; Miller, G. J.; Snyder, G. J.; Kauzlarich, S. M. High-Temperature Thermoelectric Properties of the Solid−Solution Zintl Phase $Eu_{11}Cd_6Sb_{12-x}As_x$ ($x < 3$). *Chem. Mater.* **2014**, *26*, 1393−1403.
(8) Hu, Y.; Wang, J.; Kawamura, A.; Kovnir, K.; Kauzlarich, S. M. $Yb_{14}MgSb_{11}$ and $Ca_{14}MgSb_{11}$—New Mg-Containing Zintl Compounds and Their Structures, Bonding, and Thermoelectric Properties. *Chem. Mater.* **2015**, *27*, 343−351.
(9) Sui, F.; He, H.; Bobev, S.; Zhao, J.; Osterloh, F. E.; Kauzlarich, S. M. Synthesis, Structure, Thermoelectric Properties, and Band Gaps of Alkali Metal Containing Type I Clathrates: $A_8Ga_8Si_{38}$ (A = K, Rb, Cs) and $K_8Al_8Si_{38}$. *Chem. Mater.* **2015**, *27*, 2812.
(10) Kazem, N.; Zaikina, J. V.; Ohno, S.; Snyder, G. J.; Kauzlarich, S. M. Coinage-Metal-Stuffed $Eu_9Cd_4Sb_9$: Metallic Compounds with Anomalous Low Thermal Conductivities. *Chem. Mater.* **2015**, *27*, 7508−7519.
(11) May, A. F.; McGuire, M. A.; Ma, J.; Delaire, O.; Huq, A.; Custelcean, R. Properties of single crystalline AZn_2Sb_2 (A = Ca,Eu,Yb). *J. Appl. Phys.* **2012**, *111*, 033708.
(12) Toberer, E. S.; May, A. F.; Melot, B. C.; Flage-Larsen, E.; Snyder, G. J. Electronic structure and transport in thermoelectric compounds AZn_2Sb_2 (A = Sr, Ca, Yb, Eu). *Dalton Trans.* **2010**, *39*, 1046−1054.
(13) Zhang, H.; Fang, L.; Tang, M.-B.; Man, Z. Y.; Chen, H. H.; Yang, X. X.; Baitinger, M.; Grin, Y.; Zhao, J.-T. Thermoelectric properties of $Yb_xEu_{1-x}Cd_2Sb_2$. *J. Chem. Phys.* **2010**, *133*, 194701.
(14) Fleurial, J. P.; Gailliard, L.; Triboulet, R.; Scherrer, H.; Scherrer, S. Thermal properties of high quality single crystals of bismuth telluride—Part I: Experimental characterization. *J. Phys. Chem. Solids* **1988**, *49*, 1237−1247.
(15) Kazem, N.; Hurtado, A.; Sui, F.; Ohno, S.; Zevalkink, A.; Snyder, J. G.; Kauzlarich, S. M. High Temperature Thermoelectric Properties of the Solid-Solution Zintl Phase $Eu_{11}Cd_{6-x}Zn_xSb_{12}$. *Chem. Mater.* **2015**, *27*, 4413−4421.
(16) Ribeiro, R. A.; Avila, M. A. Single crystal flux growths of thermoelectric materials. *Philos. Mag.* **2012**, *92*, 2492−2507.
(17) Sheldrick, G. M. A short history of SHELX. *Acta Crystallogr., Sect. A: Found. Crystallogr.* **2008**, *64*, 112−122.
(18) Petricek, V.; Dusek, M.; Palatinus, L. Crystallographic Computing System JANA2006: General features. *Z. Kristallogr. - Cryst. Mater.* **2014**, *229*, 345−352.
(19) Saparov, B.; Bobev, S.; Ozbay, A.; Nowak. Synthesis, structure and physical properties of the new Zintl phases $Eu_{11}Zn_6Sb_{12}$ and $Eu_{11}Cd_6Sb_{12}$. *J. Solid State Chem.* **2008**, *181*, 2690.
(20) Saparov, B.; Saito, M.; Bobev, S. Syntheses, and crystal and electronic structures of the new Zintl phases Na_2ACdSb_2 and K_2ACdSb_2 (A = Ca, Sr, Ba, Eu, Yb): Structural relationship with Yb_2CdSb_2 and the solid solutions $Sr_{2-x}A_xCdSb_2$, $Ba_{2-x}A_xCdSb_2$ and $Eu_{2-x}Yb_xCdSb_2$. *J. Solid State Chem.* **2011**, *184*, 432−440.
(21) Miller, G. J. The "Coloring Problem" in Solids: How It Affects Structure, Composition and Properties. *Eur. J. Inorg. Chem.* **1998**, *1998*, 523−536.
(22) Momma, K.; Izumi, F. VESTA 3 for three-dimensional visualization of crystal, volumetric and morphology data. *J. Appl. Crystallogr.* **2011**, *44*, 1272−1276.
(23) Xia, S.-q.; Bobev, S. Cation−Anion Interactions as Structure Directing Factors: Structure and Bonding of Ca_2CdSb_2 and Yb_2CdSb_2. *J. Am. Chem. Soc.* **2007**, *129*, 4049−4057.
(24) Cao, Q.-G.; Zhang, H.; Tang, M.-B.; Chen, H.-H.; Yang, X.-X.; Grin, Y.; Zhao, J.-T. Zintl phase $Yb_{1-x}Ca_xCd_2Sb_2$ with tunable thermoelectric properties induced by cation substitution. *J. Appl. Phys.* **2010**, *107*, 053714.
(25) Ohno, S.; Zevalkink, A.; Takagiwa, Y.; Bux, S. K.; Snyder, G. J. Thermoelectric properties of the $Yb_9Mn_{4.2-x}Zn_xSb_9$ solid solutions. *J. Mater. Chem. A* **2014**, *2*, 7478−7483.
(26) Mantina, M.; Valero, R.; Cramer, C. J.; Truhlar, D. G. Atomic Radii of the Elements. In *CRC Handbook of Chemistry and Physics*, 94 ed.; Haynes, W. M., Ed.; CRC Press: London, 2013.
(27) Lee, K.; Kaseman, D.; Sen, S.; Hung, I.; Gan, Z.; Gerke, B.; Pöttgen, R.; Feygenson, M.; Neuefeind, J.; Lebedev, O. I.; Kovnir, K. Intricate Short-Range Ordering and Strongly Anisotropic Transport Properties of $Li_{1-x}Sn_{2+x}As_2$. *J. Am. Chem. Soc.* **2015**, *137*, 3622−3630.
(28) Kim, H.-S.; Gibbs, Z. M.; Tang, Y.; Wang, H.; Snyder, G. J. Characterization of Lorenz number with Seebeck coefficient measurement. *APL Mater.* **2015**, *3*, 041506.

DOI: 10.1021/acs.inorgchem.6b01947
Inorg. Chem. XXXX, XXX, XXX−XXX